

Simulation of muon radiography for monitoring CO₂ stored in a geological reservoir

J. Klinger^{a,*}, S.J. Clark^b, M. Coleman^c, J.G. Gluyas^d, V.A. Kudryavtsev^a, D.L. Lincoln^e, S. Pal^a, S.M. Paling^f, N.J.C. Spooner^a, S. Telfer^a, L.F. Thompson^a, D. Woodward^a

^aDepartment of Physics and Astronomy, University of Sheffield, Sheffield, S3 7RH, UK

^bDepartment of Earth Sciences, Durham University, Durham, DH1 3LE, UK

^cNASA Jet Propulsion Laboratory, California Institute of Technology, Pasadena, California, USA

^dDurham Energy Institute, Durham University, Durham, DH1 3LE, UK

^eDepartment of Civil and Structural Engineering, University of Sheffield, Sheffield, S1 3JD, UK

^fSTFC Boulby Underground Science Facility, Boulby Mine, Cleveland, TS13 4UZ, UK

Abstract

Current methods of monitoring subsurface CO₂, such as repeat seismic surveys, are episodic and require highly skilled personnel to acquire the data. Simulations based on simplified models have previously shown that muon radiography could be automated to continuously monitor CO₂ injection and migration, in addition to reducing the overall cost of monitoring. In this paper, we present a simulation of the monitoring of CO₂ plume evolution in a geological reservoir using muon radiography. The stratigraphy in the vicinity of a nominal test facility is modelled using geological data, and a numerical fluid flow model is used to describe the time evolution of the CO₂ plume. A planar detection region with a surface area of 1000 m² is considered, at a vertical depth of 776 m below the seabed. We find that one year of constant CO₂ injection leads to changes in the column density of $\lesssim 1\%$, and that the CO₂ plume is already resolvable with an exposure time of less than 50 days.

Keywords: Muon radiography, CCS, Carbon capture monitoring, Carbon capture, Cosmic-ray muons

1. Introduction

The regulation of atmospheric greenhouse gas concentrations is required to stabilise the effects of anthropogenic climate change. Most scenarios of economic development predict a steep rise in greenhouse gas concentrations due to an increase in demand for energy, and hence fossil fuel usage [1]. The option of CO₂ Capture and Storage (CCS) is regarded as one technological solution for atmospheric CO₂ mitigation [2]. CCS technologies have the capacity to reduce CO₂ emissions from power stations by up to 90% [3], by the injection of liquefied CO₂ into on-shore or off-shore geological repositories for permanent storage.

The principle of transporting and storing CO₂ in depleted oil fields or saline formations is already well understood, although there are technological and commercial issues which need to be addressed [4]. In particular, there is a demand for a continuous and economically viable method for monitoring the injection and migration of subsurface CO₂. The migration of subsurface fluids can be highly unpredictable, even in developed oil fields [5]. Current monitoring methods are episodic and require highly skilled personnel to acquire the data. Such technologies include repeat seismic surveys, measuring the subsurface response to electromagnetic waves, measuring specific gravity and monitoring pressure [6]. Any new, and preferably low-cost, technology which is able to provide automated and continuous

monitoring will greatly enhance the long-term viability of CCS technologies. One such option that has been proposed is muon radiography [7].

High-energy muons, which are produced due to the interactions of cosmic-rays with the Earth's upper atmosphere, are deeply penetrating charged particles. Muons are point-like charged particles which are very similar to electrons, but have a rest mass approximately 200 times that of the electron. All charged particles interact with other charged particles via the electromagnetic interaction. In this paper we consider muons interactions within matter, through which they are travelling. Although the materials in the Earth are electrically neutral, the atoms within the materials are composed of positively charged nuclei and negatively charged electrons. When charged particles, such as cosmic-ray muons, interact with nuclei and electrons they scatter and lose energy by ionising and exciting atoms, as well as occasionally producing secondary particles that will be absorbed in matter quickly. As with any stochastic energy transfer in a bulk material, the energy is eventually dispersed as heat.

There are other cosmic-ray particles which one can consider at the surface of the Earth. Other point-like cosmic-ray particles such as electrons and photons¹ lose energy at a much faster rate compared to muons underground, due having a significantly lower rest mass (or zero rest mass in the case of the

¹ Although photons are electrically neutral particles, they are the 'force-carriers' of the electromagnetic interaction, and therefore by definition interact with electrically charged particles.

*Corresponding author

Email address: j.klinger@sheffield.ac.uk (J. Klinger)

photon) compared to muons. Cosmic-ray particles which have a more complex internal structure (and are therefore not point-like) such as protons, neutrons, mesons and nuclei can additionally interact in the Earth via hadronic interactions. This additional interaction significantly reduces their range underground compared to muons. Therefore muons are the only charged particles produced in the atmosphere which are observed in experiments based in underground observatories. There is a relatively large flux of neutrinos underground, although their extremely low interaction probability means that they can be neglected.

Muons lose energy as they traverse dense materials and, once they have a sufficiently low energy, will stop and be absorbed into the material or decay to produce an electron which will also be absorbed. Muon energy loss is fundamentally related to the density of the medium through which they travel. It is also related to the mean atomic number and weight of the bulk material through which they pass. It is therefore possible to map the density profile of a large object by observing local variations in the flux of muons emerging from the target object.

Muon radiography is already used for a wide variety of monitoring purposes, from relatively small-scale applications such as the monitoring of cargo containers for high-Z materials² [8–11], to the mapping of density variations in large-scale structures such as voids in the ancient pyramids [12] and magma chambers in volcanoes [13, 14]. Recent research has shown that muon radiography may be able to provide a low-cost, continuous subsurface CO₂ monitoring system for the injection and subsequent movement of CO₂, as an alternative or complementary system to seismic technology [7].

In this paper, we will show the results of the first detailed simulation of muon radiography for this application. Our model incorporates geological data to describe a subsurface CO₂ storage site, with a realistic model of subsurface CO₂ plume evolution. Such models will be an essential part of any future use of this technology. The experience of fluid injection processes in the oil industry suggests that natural systems do not necessarily behave as anticipated. An example of this is the use of waterflood to enhance oil production, which can lead to the rapid breakthrough of water without oil [5]. Thus, in the context of CCS, it will be essential to have a detailed model of expected behaviour so that deviations from those expectations can be identified at the earliest stage.

It is clear that muon radiography will not be able to image subsurface CO₂ with a higher resolution than technologies such as seismic surveying. We propose, however, that muon radiography will be sufficiently accurate such that it may reduce the total cost associated with CCS, if used in combination with existing technology. Therefore the utility of muon radiography as a tool to monitor subsurface CO₂ will ultimately depend upon the practicality of deployment of the technology at CO₂ injection sites and the cost of deployment relative to other monitoring technology which could be used. We will discuss these aspects in more detail in Section 8.

²The monitoring of high-Z materials typically utilises the large scattering angle of muons incident on high mass nuclei, rather than changes in the muon flux due to muon attenuation, although Ref. [8] also uses muon disappearance.

We will show that this technology is conceptually viable, and as such this paper represents a crucial milestone in the realisation of muon radiography for the purpose of CCS.

2. Conceptual overview

Projected implementations of CO₂ capture technologies utilise pre-combustion, post-combustion [15] or oxyfuel processes [16, 17]. Independent of the setup, liquefied or supercritical CO₂ can be subsequently piped to an on-shore or off-shore geological storage site, of which there are already numerous examples [4]. In the context of this paper we consider off-shore sites, which may be more commercially attractive due to the prospect of enhanced oil recovery [18, 19].

In the current examples of this technology, liquefied or supercritical CO₂ is injected underground via a vertical well to a geological reservoir. It is required that the reservoir is sealed by an impermeable stratum (‘cap-rock’), in order to contain the subsurface CO₂ volume, which will rise under buoyancy forces.

In this work, the geological storage reservoir considered is a saline aquifer, although the simulation procedures would be similar for a depleted oil or gas field with residual hydrocarbons and brine. As a consequence of constant CO₂ injection, the density distribution of the reservoir will evolve. To model this, we use a numerical multiphase fluid flow model, which we describe in detail in Section 4, following the approach of Refs. [20, 21]. The model describes the vertical and horizontal distribution of CO₂ at discrete time steps, which evolves spatially from the CO₂ injection point. Crucially, the model computes the change in the local density due to CO₂ and brine distributions within the reservoir. As a result of the evolving density profile, which alters the survival probability of passing muons, one should expect localised modifications to the muon flux at depths below the storage reservoir.

We propose that muon detectors are placed in containers that meet standard dimensions used for oil-well boreholes. Full details of the detector dimensions are given in Section 6. The detectors are assumed to be deployed in horizontal arrays below the reservoir, such that each array of detectors is fully contained within a surface area of approximately 1000 m². We assume for this study that each borehole container will contain a number of bars of plastic scintillator. Plastic scintillators, which emit light in response to the energy depositions of charged particles such as muons, are a low-cost and durable technology which is widely used in particle physics research.

Given the relatively low flux of muons at the depths which are considered in this study, we employ a simple imaging strategy. We propose to resolve changes in the density of the total geological section via the change of the underground muon count due to CO₂ injection. Any background to the muon signals underground can easily be suppressed by requiring a minimum number of scintillator bar hits. As the effect of CO₂ injection underground is to reduce the overall density of the aquifer, one can measure an enhancement of the number of muons below the reservoir, with respect to the number of muons that one would expect in the absence of subsurface CO₂.

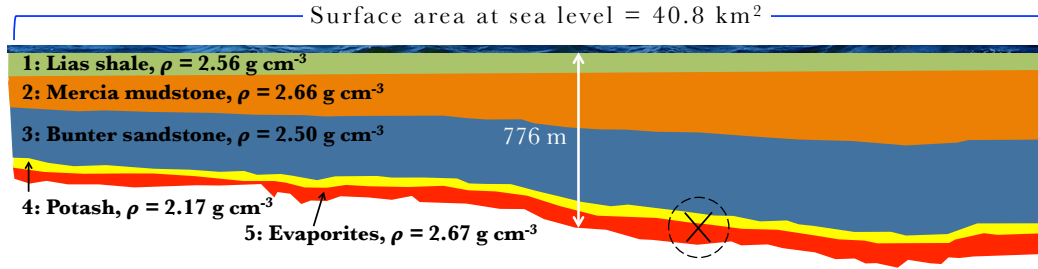


Figure 1: A diagram of geological stratigraphy model used in this simulation. The layer number, simplified composition and average bulk density is indicated for each layer. There is additionally a layer of sea water above layer 1, with a depth of 32 m. Layer ‘3’ corresponds to the saline aquifer, which is a suitable storage medium for CO₂. The approximate location of the proposed detector site is indicated by the ‘X’ symbol. In this simulation, CO₂ is piped underground via a vertical well, with the point of injection vertically above the detector site.

3. Geological modelling

An unfaulted geocellular model of the geology in the region of Boulby Mine, situated in Cleveland, United Kingdom, has been produced for this study. There are a number of reasons why we have performed the simulation at this location, despite the site not being an option for off-shore CCS. Firstly, the geology of the site at Boulby is well understood. The stratigraphy features a permian evaporite layer at a depth of 0.75–1.1 km, which is typical of geological repository sites. Furthermore, there is safe, supported and versatile access provided by Israel Chemicals Ltd UK, who operate a commercial facility in Boulby Mine, and the STFC Boulby Underground Science Facility [22], which allows for comprehensive testing of prototype detectors in the underground environment.

The geocellular model describes five strata below sea level, with a detector situated 776 m below the seabed, which is the approximate depth of a proposed subsurface muon detector test-site. The five strata are referred to sequentially as ‘layer 1’, with the shallowest depth, to ‘layer 5’, with the greatest depth. There is additionally a layer of seawater above layer 1, with a depth of 32 m vertically above the test-site. The data sample which is used to describe the geological stratigraphy of this site is described in Section 3.1, and the parameters which are used to describe the saline aquifer, as a hypothetical CO₂ storage site, are described in Section 3.2.

Figure 1 depicts the model of the stratigraphy used in this simulation. The approximate location of the detector site is indicated in the figure. The implementation of the geological composition and strata boundary (‘horizon’) data in the simulation framework is described in Section 5.1.

3.1. Data sample

Data describing four seismic horizons have been provided by Israel Chemicals Ltd UK. These horizons correspond to the top of layer 1 (the seabed), the top horizon of layer 4, the common horizon of layers 4 and 5, and the bottom horizon of layer 5. In order to represent the stratigraphy of layers 1–3, two additional layers were added to the model, based on the estimated thickness taken from well data.

The horizon data are converted into a triangular-based mesh in order to reduce CPU and memory overheads. The average distance between points on the mesh is approximately 100 m, which represents the level of accuracy of this model. The horizon data are combined with information describing the composition of each layer. The average bulk density and simplified composition of each layer are indicated in Figure 1. This information is used to populate each layer in the simulation described in Section 5.

3.2. Reservoir data

A numerical model is employed to describe the injection of CO₂ and the subsequent density evolution of the geological reservoir. The typical properties of the storage reservoir, which are required to parameterise the model, are described in this section.

The numerical model, which is described in detail in Section 4, is based on a system of equations which define a uniform axisymmetric region of the geological reservoir which fully contains the volume of subsurface CO₂. The fraction of the reservoir containing void spaces, initially occupied by the *in situ* brine, is given by the porosity ϕ . The injected CO₂ is entirely confined above and below by impermeable horizontal boundaries, separated by a distance H . This also defines the height of the CO₂ injection well boundary, which is centred on the axis with a radius r . A constant mass-rate of CO₂ injection, M_n , is imposed which outwardly displaces the *in situ* brine.

Accurate equations of state [23, 24] are used with reference values of pressure and temperature for the reservoir system, in order to determine the corresponding fluid properties as listed in Table 1. The rock intrinsic density and porosity values are determined from a log of the test storage sandstone layer at the site of Boulby Mine, Cleveland, United Kingdom. The parameters which follow are typical experimental values characterising a sandstone-brine-CO₂ system following the study of Ref. [25], where further descriptions of their meaning are also given. Typical values for well depth below an impermeable boundary and well radius are given along with a feasible mass-rate of injection, which is at a lower limit of valuation deemed practical (3–120 kg/s) for commercial CCS purposes [26].

Table 1: The parameters used to model the CO₂ injection and multiphase interactions in the geological reservoir presented in this analysis. All parameters are assumed to have typical values, except for those indicated by ‘*’, which have been acquired from data provided by Israel Chemicals Ltd UK.

Parameter	Sym.	Value	Units
Brine density	ρ_w	1100	kg/m ³
Brine viscosity	μ_w	900	$\mu\text{Pa s}$
Brine bulk modulus	K_w	2.90	GPa
CO ₂ density	ρ_n	720	kg/m ³
CO ₂ viscosity	μ_n	60.0	$\mu\text{Pa s}$
CO ₂ bulk modulus	K_n	0.025	GPa
Reservoir rock intrinsic density (*)	ρ_s	2670	kg/m ³
Porosity (*)	ϕ	0.15	-
Permeability	\mathbf{k}	1.875×10^{-13}	m ²
Brine residual saturation	S_{rw}	0.4438	-
CO ₂ end-point relative permeability	k_{rn}	0.3948	-
Brine relative permeability exponent	m_k	3.2	-
CO ₂ relative permeability exponent	n_k	2.6	-
van Genuchten parameter	m_v	0.46	-
van Genuchten parameter	p_v	19.6	kPa
Well/reservoir height	H	170	m
Well radius	r	0.2	m
CO ₂ mass-rate of injection	M_n	20	kg/s

4. Numerical subsurface CO₂ simulation

Numerical models are widely used in order to solve large-scale fluid flow problems in porous media. In this section, we will present the formulation and implementation of a numerical model for the simulation of a geological storage reservoir over discrete time steps after the start of a period of constant CO₂ injection. This model will then be used in Section 5.3 to assess to what extent bulk density changes in such a system can be tracked over time using muon radiography.

We present a simple numerical model based on the coupled theoretical approach of Ref. [21]. The model is then embedded into our GEANT4-based simulation³ [27], described in Section 5, in order to account for the coupled interaction of CO₂ and brine within the reservoir, and hence the corresponding macroscopic changes in composition and density.

In Section 4.1, we formulate the numerical model which we will use to generate subsurface CO₂ plume formations, using the input parameters described in Section 3.2. The bulk density distribution of the reservoir after CO₂ injection, which represent the solutions of this model, are discussed further in Section 4.2.

One should note that we only intend for the model to be used in this simulation of muon radiography for the application of mapping density changes in a large overburden. It is not intended that this model could be used for predictive purposes

³ GEANT4 is a simulation toolkit for modelling interactions and transport of elementary particles in matter, which is used widely in the field of high energy physics.

at this site. The site that we model is anyway unsuitable for CO₂ storage, rather it represents a site for which a complete dataset was available and, as discussed in Section 3, contains a serviced laboratory for testing prototype detectors.

4.1. Mathematical formulation

The storage of CO₂ in a deep saline aquifer, generally of moderate to high temperatures and pressures, presents a two-phase fluid system within the host rock; namely a ‘non-wetting’ and ‘wetting’ phase. The non-wetting phase, modelled as a supercritical or liquid CO₂-rich fluid, displaces the wetting-phase, which is modelled as a liquid H₂O-rich fluid, within a porous solid (rock) phase.

We assume that bulk composition and density changes are primarily due to the multiphase displacing and drainage behaviour within the reservoir system. We therefore concentrate on modelling the saturation effects, whilst neglecting the multiphase miscibility, thermal, inertial and solid deformation effects, which is typical for a first-order reservoir analysis.

Considering the continuity of multiple fluid phases in a porous medium, the following general macroscopic mass balance equation is given for each phase π ,⁴

$$\frac{\partial(\phi S_\pi \rho_\pi)}{\partial t} + \nabla \cdot (\phi S_\pi \rho_\pi \mathbf{v}_\pi) = 0, \quad (1)$$

where ϕ is porosity (the fraction of void volume to total volume), S_π is fluid saturation (the fraction of fluid phase volume to void volume, such that $\sum_\pi S_\pi = 1$), ρ_π is intrinsic phase density and \mathbf{v}_π is velocity. The relevant constitutive relationships for bulk fluid compressibility and flow respectively are:

$$\frac{1}{\rho_\pi} \frac{\partial \rho_\pi}{\partial t} = \frac{1}{K_\pi} \frac{\partial p_\pi}{\partial t} \quad \text{and} \quad \phi S_\pi \mathbf{v}_\pi = \frac{k_{r\pi} \mathbf{k}}{\mu_\pi} (-\nabla p_\pi + \rho_\pi \mathbf{g}), \quad (2)$$

where K_π is bulk modulus, p_π is fluid pressure, \mathbf{g} is the gravity vector, and \mathbf{k} , $k_{r\pi}$ and μ_π are the extended Darcy’s law terms, for multiphase flow of intrinsic rock permeability, relative permeability and dynamic viscosity respectively. The constitutive relationships are substituted into Equation (1) by assuming ϕ constant and dividing through by ρ_π , whilst neglecting the gradient of ρ_π , giving

$$\frac{\phi S_\pi}{K_\pi} \frac{\partial p_\pi}{\partial t} + \phi \frac{\partial S_\pi}{\partial t} + \nabla \cdot \left[\frac{k_{r\pi} \mathbf{k}}{\mu_\pi} (-\nabla p_\pi + \rho_\pi \mathbf{g}) \right] = 0. \quad (3)$$

The fluid saturation capacity relationship is introduced:

$$\frac{\partial S_w}{\partial t} = \frac{\partial S_w}{\partial p_c} \frac{\partial p_c}{\partial t} = \frac{\partial S_w}{\partial p_c} \left(\frac{\partial p_n}{\partial t} - \frac{\partial p_w}{\partial t} \right), \quad (4)$$

where $S_w(p_c)$ is the saturation of the wetting phase, which is controlled by the capillary pressure p_c . The capillary pressure is defined as the difference in pressure between the non-wetting and wetting phases, $p_c = p_n - p_w$.

⁴In this formulation $\pi = n, w$, which subscript the terms belonging to the non-wetting and wetting phases respectively.

Employing (3) for both fluid phases gives two coupled equations on instating the appropriate fluid subscripts. Finally, substituting (4) into the coupled equations resolves the fluid pressures as the primary variables. In order to solve this system of equations, they are cast into the following spatially discretised form by employing the standard Galerkin finite element procedure [28], within the domain Ω and on its boundary Γ , for which the usual initial and boundary conditions are incorporated [21]:

$$\begin{bmatrix} \mathbf{C}_w & \mathbf{Q} \\ \mathbf{Q}^T & \mathbf{C}_n \end{bmatrix} \frac{d}{dt} \begin{Bmatrix} \mathbf{p}_w \\ \mathbf{p}_n \end{Bmatrix} + \begin{bmatrix} \mathbf{H}_w & \mathbf{0} \\ \mathbf{0} & \mathbf{H}_n \end{bmatrix} \begin{Bmatrix} \mathbf{p}_w \\ \mathbf{p}_n \end{Bmatrix} = \begin{Bmatrix} \mathbf{f}_w \\ \mathbf{f}_n \end{Bmatrix} \quad (5)$$

where

$$\begin{aligned} \mathbf{C}_\pi &= \int_{\Omega} \mathbf{N}^T \left(\frac{\phi S_\pi}{K_\pi} - \phi \frac{\partial S_w}{\partial p_c} \right) \mathbf{N} d\Omega, \\ \mathbf{Q} &= \int_{\Omega} \mathbf{N}^T \left(\phi \frac{\partial S_w}{\partial p_c} \right) \mathbf{N} d\Omega, \\ \mathbf{H}_\pi &= \int_{\Omega} (\nabla \mathbf{N})^T \frac{k_{r\pi} \mathbf{k}}{\mu_\pi} \nabla \mathbf{N} d\Omega, \\ \mathbf{f}_\pi &= \int_{\Omega} (\nabla \mathbf{N})^T \frac{k_{r\pi} \mathbf{k}}{\mu_\pi} \rho_\pi \mathbf{g} d\Omega - \int_{\Gamma} \mathbf{N}^T \frac{q_\pi}{\rho_\pi} d\Gamma, \end{aligned} \quad (6)$$

are compressibility, coupling, permeability and supply matrices respectively. The \mathbf{N} terms are a set of linear shape functions interpolating over the discretised domain. The mass flux, q_π , imposed normal to the boundary, is also introduced as a consequence of the boundary conditions.

To model the injection scenario, the system of equations (5) are solved with the following specific boundary conditions. The inner (inflow) vertical injection boundary is prescribed with a mass-flux boundary condition, q_n , which is related to the mass-rate of CO_2 injection by $M_n = q_n 2\pi r H$. At the outer (outflow) radial extent of the domain, a constant hydrostatic pressure far-field boundary condition is prescribed. Otherwise, no-flux boundary conditions are assumed.

This system of equations is non-linear due to the dependence of the coefficient matrices on the primary variables; namely, the saturation and relative permeability terms, $S_\pi(p_c)$ and $k_{r\pi}(S_\pi)$. These relationships are determined experimentally for a given system and are parametrised in this work by the van Genuchten S_π - p_c model [29] and by a power law $k_{r\pi}$ - S_π relationship [25], respectively (see Table 1). The model parameters, ϕ , \mathbf{k} , ρ_π , μ_π and K_π are assumed constant and uniform, which is typical for basic hydro-geological investigations.

Once the primary pressure variables are determined for a given point in time, the corresponding secondary saturation variables $S_\pi(p_c)$ are determined. From this, the following macroscopic bulk density can be given by summing the intrinsic phase densities multiplied by their corresponding volume fractions,

$$\rho_b = (1 - \phi)\rho_s + \phi S_n \rho_n + \phi S_w \rho_w, \quad (7)$$

which introduces the intrinsic density of the solid rock/minerals, ρ_s .

The spatial integrations of (6) are carried out using Gaussian quadrature. The temporal integration of (5) is carried out using finite differencing; the set of equations are solved monolithically using a fully implicit (unconditionally stable) embedded scheme producing solutions of adjacent order in accuracy to allow for error control and adaptive time-stepping. This is considered appropriate given that a coupled injection scenario is being modelled. Each time-step is solved iteratively due to the non-linearities, which is done via an accelerated fixed-point type procedure until convergence is met. The linearised system is solved at each iteration by a standard direct multi-frontal solver. Further details on the implementation of a system of equations of this type are given in Refs. [21, 28, 30].

4.2. Reservoir bulk density distribution

The solutions to the model presented in Section 4.1 describe the density distribution of the reservoir at time t after the start of continuous CO_2 injection. The radial extent $r_E(t)$ of the expanding volume of CO_2 has the relationship $r_E \propto \sqrt{t}$ [31].

It is found that density changes of $\lesssim 4\%$ are expected due to the presence of injected CO_2 , with respect to the bulk density of the reservoir pre-injection. For the purposes of muon radiography, which is sensitive to the density of the total geological section, this corresponds to a change in the total column density of $\lesssim 1\%$. In Section 5, Figure 2 shows a graphical representation of the subsurface bulk density distribution at a specific point in time. This distribution is subsequently interfaced with GEANT4, following the voxelisation procedure presented in Section 5.2.

5. Simulation framework

The simulation framework that is used for muon transport, in which muons descend through the geological model from Section 3, is described in this section. All stages of the simulation are performed within the GEANT4.9.6 framework [27]. In Section 5.1, we present the strategy that we employ for converting the geological data to GEANT4 volumes. In Section 5.2, we describe the implementation of the density distribution, ρ_b , of the reservoir due to the presence of CO_2 . In Section 5.3, we present the modelling of the muon flux distribution that we use at sea level, and the subsequent transport to the detector site.

5.1. Geological stratigraphy interfacing

The model of the stratigraphy of the test-site presented in Section 3 is interfaced with GEANT4. The implementation of the geological model in GEANT4 is highly CPU and memory intensive, so steps are taken to reduce such overheads.

In the simulation, each stratum of rock is constructed independently from one another within GEANT4, which allows for multi-threading to be used in order to reduce total computation time. We construct each stratum of rock using two parallel (and very approximately horizontal) meshes, bound by four vertical faces. Each mesh represents one of the horizons described in Section 3. We opt to construct the less detailed horizons using quadrangular-based meshes and the highly detailed horizons using triangular-based meshes.

The muon transport simulation, which is described in detail in Section 5.3, is performed in two stages: firstly only transporting muons to the lower horizon of layer 2 (or, equivalently, the top horizon of layer 3); and in a subsequent stage of simulation, transporting muons through the remaining three layers. One reason for this, in addition to a general improvement in CPU performance, is that fewer constructed strata are used in GEANT4, which therefore reduces the memory overhead. Furthermore, as the first stage of the simulation only considers muons above the subsurface CO₂ formation, it is sufficient to perform this stage of the simulation only once and then perform the second stage of the simulation once for each time step of subsurface CO₂ migration.

5.2. Subsurface bulk density voxelisation

The numerical model describing the variation in bulk density of the reservoir, presented in Section 4, is implemented in the simulation using the voxelisation capabilities of GEANT4. In this framework, a regular grid of voxels (each of size $\{10 \times 10 \times 10\}$ m³) populates the domain of interest, which is rendered and parameterised by the numerical model.

We take steps to preserve the accuracy of the numerical model in the voxelisation procedure, particularly in regions of high numerical gradients caused by the fluid interface, which are due to the displacing behaviour of the CO₂. The first stage of the procedure is to overlay the finite element mesh, which describes density profile and gradient with high precision, onto the voxel grid. The voxels are then parameterised with the composition and density outputs, which are interpolated from the finite element mesh at all of the overlapping voxel centroids.

The voxelisation process is carried out at selected points in time. As described in Section 4.2 and Ref. [31], the radial extent $r_E(t)$ of the CO₂ distribution expands with time t as $r_E \propto \sqrt{t}$. Accordingly, the voxelisation is performed at intervals $(2n)^2$ days which are therefore assumed to represent the reservoir state for the period between $(2n - 1)^2$ and $(2n + 1)^2$ days, where $n = 1 \rightarrow 10$. For this simulation, using the parameters presented in Table 1, the radial extent is increased by approximately 36 m at each time-step until reaching a distance of approximately 360 m from the well.

A quarter-symmetric rendering of the system bulk density as predicted at 64 days, alongside its equivalent voxelisation of density bins for implementation with GEANT4, is shown in Figure 2.

5.3. Muon flux sampling and particle transport

For the simulation of muon energy loss in solid material, we use the GEANT4.9.6 ‘shielding’ physics list [27], with the muon-nuclear interaction process explicitly included.

We have implemented a Monte Carlo generator to sample the spectrum of muon energies E at sea level, as a function of the angle θ of the muon trajectory from the zenith. The spectrum is based on the Gaisser parameterisation [32], which accounts for correlations between the θ and E due to different muon-production mechanisms in the atmosphere. The parameterisation accounts for muon energy losses in the atmosphere, which

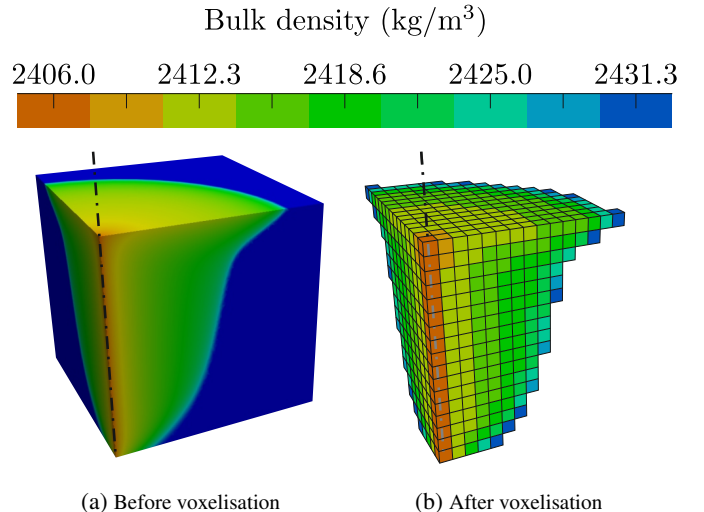


Figure 2: Quarter-symmetric rendering of the sandstone-brine-CO₂ system bulk density as predicted after 64 days (a), alongside its equivalent voxelisation of density bins for implementation with GEANT4 (b).

are very low compared to the energy losses due to interactions underground. As we describe later, we only consider muons with $E > 400$ GeV so we do not include recent measurements of the muon spectrum such as Ref. [33] in which the spectrum is only measured up to 100 GeV. Muons which have been generated according the Gaisser parameterisation and subsequently propagated to these depths have been previously shown to agree with data within $< 10\%$ [34]. We apply additional corrections to the parameterisation to account for the muon lifetime and the Earth’s curvature.

In order to reduce computation time, a number of optimisations are implemented. There are no charged particles, other than muons, which can survive through large depths of matter. Therefore any secondary particles⁵ that are produced due to the interactions of muons with matter are immediately removed from the simulation.

We only consider muons with $E > 400$ GeV and $\theta < 70^\circ$, based on a previous study of the muon survival depth [34, 35]. Given the detector depth of ~ 800 m below sea level, and that the detector array is confined to within an area of 1000 m², we require that muons originate from an approximately square region of $\{4.5 \times 4.5\}$ km² at sea-level. This surface area is sufficiently large to account for any displacement of the muon’s measured position r_{real} due to scattering during the muon transport, with respect to the position that is linearly projected from the muon’s trajectory at sea level, r_{proj} . The distribution of $|r_{\text{real}} - r_{\text{proj}}|$ of muons in this analysis are shown in Figure 3. We find that $|r_{\text{real}} - r_{\text{proj}}|$ is a steeply falling distribution, with the average displacement of muons being < 2.1 m.

As a simulated muon loses energy, we re-evaluate the muon’s maximum survival depth, d_{max} , using a look-up table. The look-

⁵ We define ‘primary’ particles as those which are present at sea level, and ‘secondary’ particles as those which are produced at any depth below this.

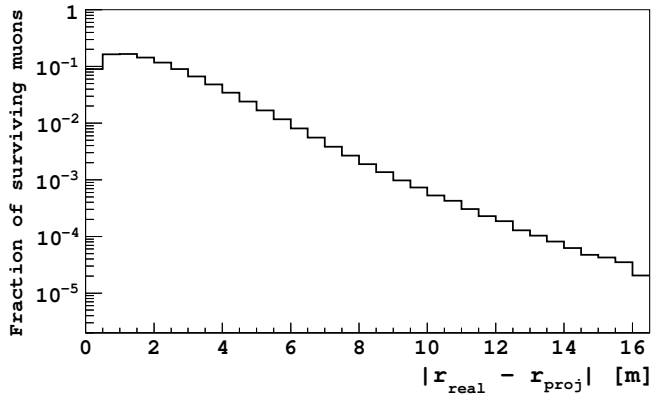


Figure 3: The distribution of $|r_{\text{real}} - r_{\text{proj}}|$ between the horizontal muon position at the detector site, r_{real} , and the position that is linearly projected from the muon’s trajectory at sea level, r_{proj} .

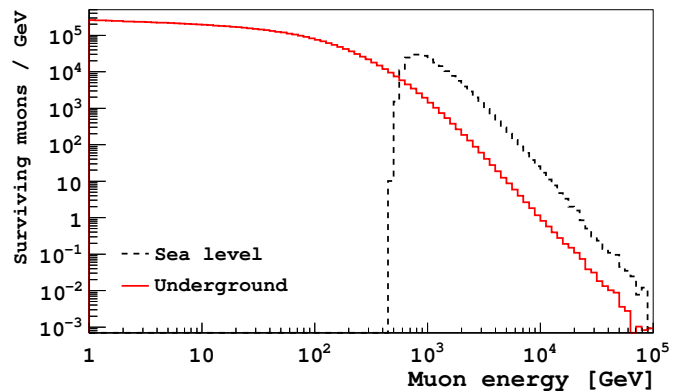


Figure 4: The energy spectra of muons, at sea level and underground respectively, for muons which survive to the detector. In total, approximately 140 days of simulation data is presented, which corresponds to approximately 2.8×10^7 muons in each spectrum. The same muons are used in both distributions, therefore only muons at sea level with energy greater than 400 GeV are observed underground.

up table, which maps E to d_{max} , is generated with the MUSIC muon simulation code [34, 35]. We then redefine d_{max} , as a function of E , as the distance beyond which a muon has a survival probability of less than 10^{-6} . The MUSIC code only considers materials with a uniform density, so we conservatively choose to evaluate d_{max} for a material with density $\rho = 2.17 \text{ g/cm}^3$, which corresponds to the lowest density of the five strata (layer 4). We therefore remove muons at any point in the simulation which have a remaining transport distance greater than d_{max} . One should note that the uniform density assumed in the MUSIC simulation code is only used to provide a conservative optimisation to the simulation and does not affect the detail of our model.

The energy spectra of muons, at sea level and underground respectively, for muons which survive to the detector are shown in Figure 4. The average energy of muons which reach the detector site is found to be approximately 1500 GeV at sea level, and 220 GeV underground. The flux of muons at the detector site is found to be approximately $2.3 \times 10^{-7} \text{ cm}^{-2} \text{ s}^{-1}$.

6. Muon detectors

In this section, we discuss the general configuration of muon detectors that we propose for mapping changes in the density of the total geological section. In the analysis of the muon simulation data, we present the maximum possible signal; therefore neglecting gaps between the detectors and assuming 100% acceptance for detecting muons whilst rejecting background from radioactivity and detector noise. The discussion presented in this section is therefore intended to provide a degree of quantification of the total efficiency of these effects, whilst still allowing us to present our results in a manner that is independent of the detector configuration.

6.1. Detector parameterisation

In order to ensure the long-term stability of the monitoring system, we assume that plastic scintillators, coupled to appropriate photo-sensors, will be employed as muon detectors for

this application. We assume that individual detectors will be confined to containers capable of being deployed in standard oil-well boreholes. The borehole containers would typically have an inner diameter of 15 cm and sufficient length (less than a few metres) for commercially available plastic scintillator bars. Plastic scintillator bars can be acquired commercially with a cross-sectional area of $\{2 \times 2\} \text{ cm}^2$ and a length of typically 100 cm. It is envisaged that multiple scintillator bars can be packed into borehole containers. The borehole containers can be deployed in a horizontal array at some depth below the reservoir.

Plastic scintillators emit light in response to charged particles, such as muons. The light signal is converted into an electrical signal with photo-sensors, such as photomultipliers, and can be subsequently digitised for analysis. The position of a muon ‘hit’ along a scintillator bar can be inferred from the time difference between signals at either end of the bar. A linear fit to multiple muon hits can be used to reconstruct a muon track. The relative position of each of the bars gives the muon angle in the plane perpendicular to the long sides of the bars. The muon’s angle in the plane parallel to the long sides of the bars can be calculated using the relative positions of the respective hits along each bar, inferred from the timing information.

From geometric arguments, the angular resolution in the plane of circular borehole faces is approximately 3° for five scintillator bar hits. Position resolution based on timing and amplitude information from optical sensors leads to an angular resolution down to 5° in the plane along the long side of the bars. We consider angular cells of $7^\circ \times 36^\circ$ in Section 7.

For this study we assume 100% trigger efficiency. The results that we present in Section 7 may be scaled accordingly, once values of trigger efficiency are acquired for a particular detector configuration. We consider a single plane of muon detectors confined within a surface area of approximately 1000 m^2 . The limiting factor for this choice of surface area is the computation

time associated with muon transport.

6.2. Detector efficiency

As there will be multiple scintillator bars per borehole container, a muon traversing a borehole container will give rise to multiple bar hits. Background signals, for example due to photo-sensor noise or radioactivity in the surrounding rock, which are assumed to be short-ranged or highly localised, can be suppressed by requiring a minimum number of bar hits $N_{\text{bar}}^{\text{hit}}$.

The efficiency for muons to satisfy the condition on $N_{\text{bar}}^{\text{hit}}$ is clearly dependent on the number and configuration of scintillator bars in the borehole containers. Furthermore, the total acceptance A for all muons in the detector region must also account for the fraction of the total surface area in the 1000 m² detector region that actually contains borehole containers. We therefore calculate the detector acceptance by considering two configuration parameters; P_{det} , the fractional surface area occupied by detectors contained within the 1000 m² region, and N_{bar} , the number of scintillator bars packed into each borehole container. We consider two values of each parameter which, for both parameters, we refer to as ‘loose’ and ‘tight’:

- $P_{\text{det}} = \{\text{loose} \sim 50\%, \text{tight} \sim 75\%\}$,
- $N_{\text{bar}} = \{\text{loose} : 16, \text{tight} : 24\}$.

It is assumed that the detectors are arranged homogeneously throughout the detector region. In reality, as discussed in Section 8, the muon detectors will be deployed in a number of boreholes (approximately 18), which extend radially from a mother borehole. Practically speaking therefore, the detectors will not be arranged in a square arrangement of approximately $\{30 \times 30\} \approx 1000$ m², as in our simulation. Instead we envisage the total instrumented area may occupy up to 1000 m². The choices of P_{det} are simply chosen to show the effect of the reducing/scaling the total number of observed muons from the maximum anticipated yield.

The arrangements of scintillator bars in the radial plane of the borehole containers, that we consider for the ‘loose’ and ‘tight’ values of N_{bar} , are shown in Figure 5. The acceptance of muons for a single plane of detectors, A , which are recorded in the detector region is shown in Figure 6, for all four combinations of P_{det} and N_{bar} . The acceptance A is shown as a function of the $N_{\text{bar}}^{\text{hit}}$, for surviving muons at the detector site crossing a single plane of detectors. Realistically, ≥ 3 bars may be required to be hit to remove radioactive background and photo-sensor noise.

7. Analysis of muon flux distribution

In this section, an analysis of the muon simulation data is performed, using muons which have been transported through the geological strata in the GEANT4 framework, as discussed in Section 5.

We propose a straightforward analysis strategy, in which we infer changes in the density of the total geological section simply from the change in the number of detected muons, with respect to the expectation in the absence of subsurface CO₂. It

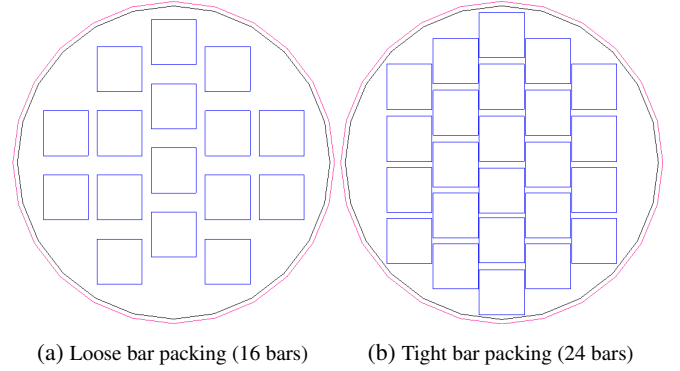


Figure 5: The arrangement of bars that we consider in this simulation, for the ‘loose’ (a) and ‘tight’ (b) values of N_{bar} .

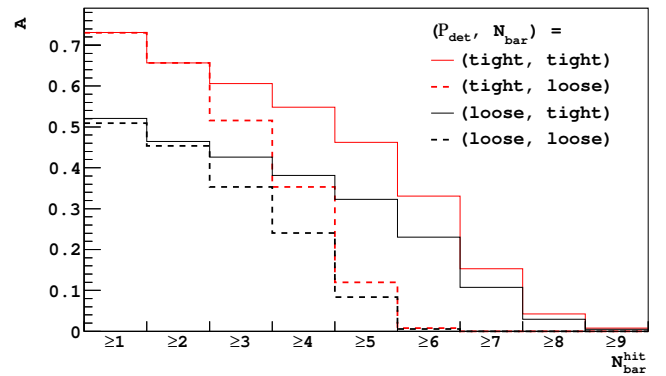


Figure 6: The acceptance of muons which are recorded in the detector region in one plane of detectors, for all four combinations of P_{det} and N_{bar} . The acceptance is shown as a function of the number of bars traversed by a muon, $N_{\text{bar}}^{\text{hit}}$.

is assumed that background noise and signals will be negligible once a condition is chosen for $N_{\text{bar}}^{\text{hit}}$.⁶ We consider increasingly large time steps in which muon data is collected, in sequential time periods since first CO₂ injection, as described in Section 5.2. This utilises the relationship between the radial extent of the CO₂ plume ($r_E \propto \sqrt{t}$), such that the time intervals correspond to periods under which the radius of the CO₂ plume is approximately constant. We parameterise the significance S of the change in the number of muons observed in a given time interval as:

$$S = \frac{N^{\text{after}} - N^{\text{before}}}{\sqrt{N^{\text{after}} + N^{\text{before}}}} \quad (8)$$

where N^{before} and N^{after} are the number of muon events observed over equal lengths of time, before any subsurface CO₂ is injected and after subsurface CO₂ is injected respectively. The number N^{before} is calculated using a statistically independent sample of muons from those used to calculate N^{after} . It is assumed that systematic uncertainties cancel in Equation 8. The

⁶There is no known effect from electrical noise, radioactivity, or other sources that can lead to an appreciable background over muons at these depths, once the requirement for $N_{\text{bar}}^{\text{hit}}$ is introduced.

denominator in Equation 8 is equal to the statistical uncertainty of the measurements.

In this analysis, both N^{before} and N^{after} refer to the number of muons detected at any point in the 1000 m² detector region. In reality, the number of muons entering this calculation is reduced primarily due to the geometric factors discussed in Section 6. The effect of the true values of the P_{det} and N_{bar} is to scale the observables N^{before} and N^{after} by an efficiency, A . It is therefore clear that S will be reduced by a factor of \sqrt{A} . We do not apply factors of \sqrt{A} to the values of S presented in this section, as realistic values of P_{det} and N_{bar} need to be investigated in further study. A degree of quantification of the acceptance A can be inferred from Figure 6.

The muon flux Φ_{μ} at each time step T , and the associated significance S (measured in standard deviations) of the change in muon count are shown in Table 2. The presented uncertainties are taken from the statistical uncertainty in the muon count. A change in the global muon flux after 49 days corresponds to approximately 24 Gaussian standard deviations. This is clearly significant even for an acceptance of $A = 5\%$.

The angular distribution of S is shown in Figures 7 and 8 for the periods 0–169 days and 169–441 days after first CO₂ injection, respectively. The shape of the plume distributions is visible above the background of statistical fluctuations, even after 25 days. Figure 9 shows the distribution of S as a function of θ only. The value of θ corresponding to the maximum value of S is shown to shift as a function of time, which is related to the dynamics of the CO₂ plume and also the sensitivity to the muon path length.

Table 2: The muon flux Φ_{μ} as a function of time step T (or equivalently the radial extent of the CO₂ plume, R) and the associated significance S relative to the muon flux prior to injection. The presented uncertainties are taken from the statistical uncertainty in the muon count.

T [days]	R [arb. units]	Φ_{μ} [$10^{-7}\text{cm}^{-2}\text{s}^{-1}$]	S
1–9	1	2.3185 ± 0.0018	0.98
9–25	2	2.3236 ± 0.0013	3.9
25–49	3	2.3278 ± 0.0010	24
49–81	4	2.3302 ± 0.0009	32
81–121	5	2.3348 ± 0.0008	40
121–169	6	2.3382 ± 0.0007	48
169–225	7	2.3410 ± 0.0006	56
225–289	8	2.3426 ± 0.0006	64
289–361	9	2.3443 ± 0.0006	72
361–441	10	2.3461 ± 0.0006	80

8. Discussion

In order to perform this simulation, we have chosen parameters which are applicable to the geology in the vicinity of Boulby Mine, Cleveland, United Kingdom. In realistic off-shore sites several parameters will change, and different analysis strategies may be adopted. This section presents a short

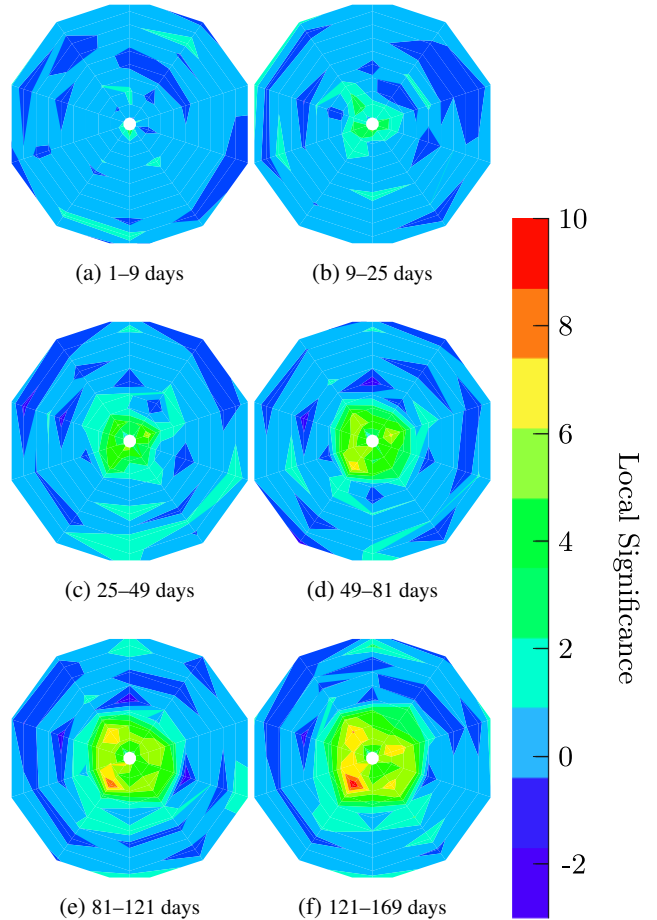


Figure 7: The significance S of the change in muon count in the detector plane due to the constant injection of subsurface CO₂, using the model described in Section 4, as a function of muon zenith and azimuthal angle θ and ψ . The caption of each figure indicates the time interval after first CO₂ injection. Each distribution contains 100 values of S , calculated in bins corresponding to $\Delta\theta = 7^\circ$ radially and $\Delta\psi = 36^\circ$ about the radial axis. A linear interpolation is used between adjacent bins.

discussion in order to provide a platform for future studies. Furthermore, we present a brief discussion on the practical viability of this technology, in particular with respect to the relative costing compared to existing technologies.

For this study we have chosen a conservative value for the mass-rate of CO₂ injection, of 20 kg/s (~ 0.63 Mtpa). Therefore it is clear that for realistic implementations of this technology, the sensitivity to both the plume extent and density variations will increase.

Clearly the depth of the CO₂ storage reservoir will vary between sites, and therefore the depth of the muon detector array will also vary between sites. Realistic off-shore sites, such as the Hewett Fields complex in the North Sea, have reservoir depths $\gtrsim 1.2$ km. Compared to the depth used in this simulation (~ 0.8 km) this corresponds to a reduction in the muon flux of 85%, based on the study presented in Ref. [34], which therefore reduces S by a factor of ~ 0.39 . This does not significantly alter

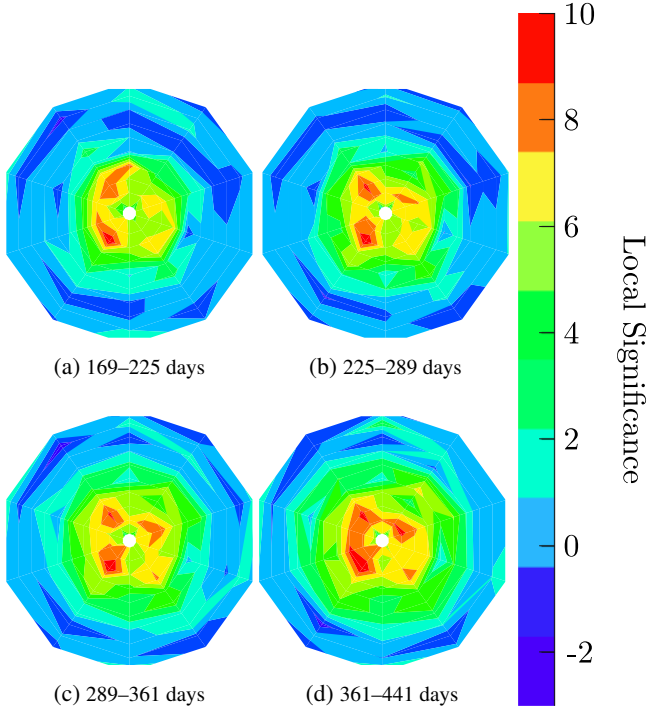


Figure 8: The significance S of the change in muon count in the detector plane due to the constant injection of subsurface CO_2 , using the model described in Section 4, as a function of muon zenith and azimuthal angle θ and ψ . The caption of each figure indicates the time interval after first CO_2 injection. Each distribution contains 100 values of S , calculated in bins corresponding to $\Delta\theta = 7^\circ$ radially and $\Delta\psi = 36^\circ$ about the radial axis. A linear interpolation is used between adjacent bins.

the conclusions of this study.

After significantly longer storage times the lateral plume size will extend well beyond what is discussed in this paper. Experience from the Sleipner CCS project [4], which operates in an offshore deep saline aquifer (depth ~ 0.8 km), suggests that CO_2 plumes may have a lateral range of approximately 15 km after 14 years. In order to image a plume with such a lateral range, one needs several arrays of muon detectors positioned at different sites relative to the injection point. Several arrays of detectors are also required to reconstruct a proper tomographic image of the CO_2 migration (in addition to the ‘line-of-sight reconstruction’). This will allow for a triangulation of the muon data, in order to reconstruct a spatially three-dimensional image of the CO_2 plume. With the detection strategy that is presented in this paper, which only uses a single detector array, one may still interpret vertical movements from unexpected changes in the angular distribution. The manner in which this process is optimised will vary from site to site.

One limiting factor, in terms of the sensitivity of this technique, is the choice of packing fraction P_{det} of the borehole containers across the total surface area of the detector array. Realistic values for this parameter are currently unclear, although this may not be important if a smaller packing fraction can be compensated by a larger area for detector deployment.

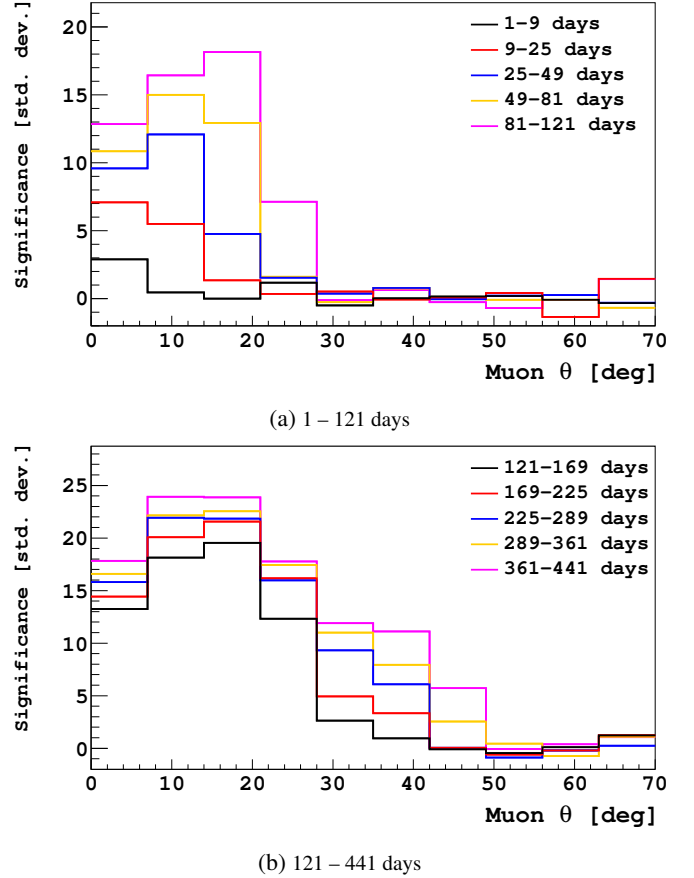


Figure 9: The significance S of the change in muon count in the detector plane due to the constant injection of subsurface CO_2 , using the model described in Section 4, as a function of muon zenith angle θ . The caption of each of the two figure indicates the time interval after first CO_2 injection.

As the effectiveness of muon radiography for the mapping of large scale objects is already proven (Ref. [12–14]), the utility of this technology will ultimately depend upon the practicality of deployment of the technology at CO_2 injection sites and the cost of deployment relative to other monitoring technology which could be used. Clearly the practicality of deployment will require further investigation. We can however provide a rough estimate of the relative cost of muon radiography, with respect to seismic technology, based on a review of freely available information and without reference to particular vendors. We choose to compare to seismic surveying, as it is clearly the most widely used monitoring technology for off-shore injection sites. The relative evaluations are based on a 2015 cost base.

Before we present our cost evaluation, we emphasise a number of points:

- Costs in this industry are volatile although relative costs, as we will discuss, are approximately fixed. Precise cost estimates are impossible on this basis.
- Multilateral sidetrack technology, which is discussed in this section, may be used for deploying the detectors, al-

though further research may yield more favourable or cost-effective methods.

- In the early stages of this technology we suggest to use modified injection wells, rather than drilling new wells for monitoring.
- Muon detector technology is expected to drop significantly in price if large-scale deployment is implemented, although the scale of this reduction is difficult to quantify.

In the few sites which have been developed for off-shore CO₂ storage [4], seismic surveys have been performed ahead of any injection and subsequently on an annual basis. The cost of such surveys varies widely and is responsive to the oil price, since most seismic data will be acquired to enable mapping of petroleum accumulations and their response to production. A typical single, modestly sized survey of around 100 km² will today cost in the region of \$5 million. For a storage site lasting 40 years this equates to \$200 million over the duration of the injection phase. This will increase further if one considers post-injection monitoring, processing and reprocessing of the annual data.

The cost to deploy muon sensors is similarly difficult to assess due to the same volatility issues on oil price. Using the same cost base we can estimate the incremental cost for deepening a well and deploying muon detectors beneath the injection site. A mid-price semi-submersible or jack-up rig for the North Sea will today cost in the region of \$300,000 per day. For the initial deployment of detectors the mobilisation and demobilisation costs will fall to the injection well itself and can be discounted for these comparison purposes. Detectors would be deployed in multilateral sidetracks drilled from the mother borehole beneath the injection site, in a process known as coiled tubing drilling [see, for instance, 36, and references therein]. Coiled tubing drilling is used extensively in off-shore settings to increase the drainage surface of well-bores into an oil reservoir. A mother borehole may have several tens of daughter boreholes. For the purpose of muon radiography, it is likely that short radii sidetracks would be drilled. We could consider 18 sidetracks (which allows for a total instrumented surface area of 1000 m²) which are each constructed over two days, plus two weeks to deploy and complete the instrumented part of the well array. This equates to about 50 days at \$300,000 or \$15 million in total.

One must then consider the cost for developing a set of detectors that would instrument the required 1000 m² area. We assume that a single detector occupies a surface area of 0.2 m², and contains approximately 25 scintillator bars, each 1 m long. With current (2015) market costs within a laboratory, one could acquire all scintillator bars (in one detector) for \$4,000, photo-sensors for \$6,000, a specially designed data acquisition system for \$2,000, other components for \$1,000 and a further \$7,000 for technical labour costs. One could envisage a cost reduction factor of at least two due to mass production - which would imply a cost of about \$10,000 per detector. Therefore in order to instrument the required 1000 m² area, this implies a cost of \$50 million. Again, the uncertainties in the precise costing at this

stage are clearly very large so this figure may rise or fall, but an estimate of the order of tens of millions of dollars is applicable. We are confident that significant cost savings will be possible by using novel and cheaper alternatives to various detector components, and a further cost reduction by mass production of detectors, when this technology becomes widely used on an industrial scale for geological repositories and CCS.

Based on experience in experimental particle physics experiments, one can expect scintillator detectors to operate for at least ten years, necessitating approximately four sets of detectors over the 40 year injection period. In practice though, seismic would still be deployed to detect plume extent in the event that the plume can be seen to be moving using muon radiography. One should note that the cost of both seismic acquisition and drilling are highly volatile and both are currently falling in line with a low oil price, however the ratio between drilling and seismic costs is effectively stable.

9. Conclusion

We have shown the results of the first detailed simulation of muon radiography for the purpose of the monitoring of sub-surface CO₂ stored in geological CCS repositories. Our model is the first to incorporate geological data to describe a sub-surface CO₂ storage site, with a simplified but nevertheless realistic modelling of CO₂ plume evolution and muon detector configuration. Non-ideal behaviour in real situations is to be expected because of geological heterogeneity or other factors, for example, variable wettability of mineral surfaces. Simulations like this will become an integral part of any future use of this CCS technology, to compare actual outcomes with the initial reservoir model.

We use a detailed numerical model of the fluid flow of sub-surface CO₂ to show that muon radiography is sensitive to the time-evolution of a CO₂ plume formation. We have shown that after approximately 49 days of constant CO₂ injection, muon radiography has a strong sensitivity to changes in column density of $\lesssim 1\%$, in the scenario that we have presented.

From our studies, it is clear that this technology is a conceptually viable monitoring method, and in combination with the study of a full prototype detector, represents a crucial milestone in the realisation of muon radiography in the context of CCS.

10. Acknowledgements

This work was supported by the Department of Energy and Climate Change and Premier Oil plc. We would like to thank the Science and Technology Facilities Council (STFC, UK) for supporting this work (grant ST/K001841/1). The studentship of D. Woodward is funded by STFC (grant ST/L502492/1). The contribution of M. Coleman was carried out in part at the Jet Propulsion Laboratory (JPL), California Institute of Technology, under contract with the National Aeronautics and Space Administration (NASA). We would like to acknowledge the continued support of Israel Chemicals Ltd UK at Boulby Mine and the team at the STFC Boulby Underground Laboratory. We

thank ENI for providing data relating to the Hewett Fields complex in the North Sea. We also thank David Jacques and Tom Lynch, from the University of Leeds, for useful discussions.

References

- [1] N. Nakicenovic and N. Swart, *Emissions Scenarios*, IPCC (2000), 570.
- [2] O. Bert Metz et al., *Carbon Dioxide Capture and Storage*, IPCC (2005), 431.
- [3] K. Stephenne, *Start-up of World's First Commercial Post-combustion Coal Fired CCS Project: Contribution of Shell Cansolv to SaskPower Boundary Dam ICCS Project*, Energy Procedia **63** (2014), 6106–6110, 12th International Conference on Greenhouse Gas Control Technologies, GHGT-12.
- [4] O. Eiken et al., *Lessons learned from 14 years of CCS operations: Sleipner, In Salah and Snøhvit*, Energy Procedia **4** (2011), 5541–5548, 10th International Conference on Greenhouse Gas Control Technologies.
- [5] B. Bailey et al., *Water control*, Oilfield Review **12** (2000), 30–51.
- [6] J. Senior et al., *Geological storage of carbon dioxide: an emerging opportunity*, Petroleum Geology Conference series **7** (2010), 1165–1169.
- [7] V. A. Kudryavtsev et al., *Monitoring subsurface CO₂ emplacement and security of storage using muon tomography*, International Journal of Greenhouse Gas Control **11** (2012), 21–24.
- [8] T. Blackwell and V. Kudryavtsev, *Development of a 3D muon disappearance algorithm for muon scattering tomography*, JINST (2015).
- [9] K. N. Borozdin et al., *Surveillance: Radiographic imaging with cosmic-ray muons*, Nature **422** (2003), 277–277.
- [10] W. C. Friedhorsky et al., *Detection of high-Z objects using multiple scattering of cosmic ray muons*, Review of Scientific Instruments **74** (2003), 4294–4297.
- [11] M. Furlan et al., *Application of muon tomography to detect radioactive sources hidden in scrap metal containers*, Advancements in Nuclear Instrumentation Measurement Methods and their Applications (ANIMMA) (2013), 1–7.
- [12] L. W. Alvarez et al., *Search for Hidden Chambers in the Pyramids*, Science **167** (1970), 832–839.
- [13] J. Marteau et al., *Muons tomography applied to geosciences and volcanology*, Nuclear Instruments and Methods in Physics Research Section A: Accelerators, Spectrometers, Detectors and Associated Equipment **695** (2012), 23–28, New Developments in Photodetection NDIP11.
- [14] N. Kanetada, *Geo-tomographic Observation of Inner-structure of Volcano with Cosmic-ray Muons*, Journal of Geography (Chigaku Zasshi) **104** (1995), 998–1007.
- [15] U. Desideri *Advanced absorption processes and technology for carbon dioxide (CO₂) capture in power plants*, vol. 1 of *Woodhead Publishing Series in Energy*. Woodhead Publishing. 2010.
- [16] P. Mathieu *Oxyfuel combustion systems and technology for carbon dioxide (CO₂) capture in power plants*, vol. 1 of *Woodhead Publishing Series in Energy*. Woodhead Publishing. 2010.
- [17] S. Kluiters et al. *Advanced oxygen production systems for power plants with integrated carbon dioxide (CO₂) capture*, vol. 1 of *Woodhead Publishing Series in Energy*. Woodhead Publishing. 2010.
- [18] M. Blunt et al., *Carbon dioxide in enhanced oil recovery*, Energy Conversion and Management **34** (1993), 1197–1204, Proceedings of the International Energy Agency Carbon Dioxide Disposal Symposium.
- [19] A. R. Awan et al., *A Survey of North Sea Enhanced-Oil-Recovery Projects Initiated During the Years 1975 to 2005*, Society of Petroleum Engineers (2015).
- [20] D. Lincoln et al., *Coupled two-component flow in deformable fractured porous media with application to modelling geological carbon storage*, Numerical Methods in Geotechnical Engineering (2014), 989–994.
- [21] R. W. Lewis and B. A. Schrefler, *The Finite Element Method in the Static and Dynamic Deformation and Consolidation of Porous Media*. John Wiley & Sons, second edition. 1998.
- [22] A. Murphy and S. Paling, *The Boulby Mine Underground Science Facility: The Search for Dark Matter, and Beyond*, Nuclear Physics News **22** (2012), 19–24, <http://dx.doi.org/10.1080/10619127.2011.629920>.
- [23] I. H. Bell et al., *Pure and Pseudo-pure Fluid Thermophysical Property Evaluation and the Open-Source Thermophysical Property Library CoolProp.*, Industrial & engineering chemistry research **53** (2014), 2498–2508.
- [24] A. M. Rowe and J. C. S. Chou, *Pressure-Volume-Temperature-Concentration Relation of Aqueous NaCl Solutions*, Journal of Chemical and Engineering Data **15** (1970), 61–66.
- [25] S. A. Mathias et al., *On relative permeability data uncertainty and CO₂ injectivity estimation for brine aquifers*, International Journal of Greenhouse Gas Control **12** (2013), 200–212.
- [26] S. A. Mathias et al., *Role of partial miscibility on pressure buildup due to constant rate injection of CO₂ into closed and open brine aquifers*, Water Resources Research **47** (2011).
- [27] S. Agostinelli et al., *Geant4 - a simulation toolkit*, Nucl.Instrum.Meth **506** (2003), 250–303.
- [28] O. C. Zienkiewicz et al. *The Finite Element Method Fifth edition Volume 1: The Basis*, vol. 1. Butterworth-Heinemann, Oxford, 6 edition. 2005.
- [29] M. T. van Genuchten, *A Closed-form Equation for Predicting the Hydraulic Conductivity of Unsaturated Soils*, Soil Science Society of America Journal **44** (1980), 892–898.
- [30] K.-J. Bathe *Finite Element Procedures*. Prentice Hall. 1995.
- [31] J. M. Nordbotten et al., *Injection and Storage of CO₂ in Deep Saline Aquifers: Analytical Solution for CO₂ Plume Evolution During Injection*, Transport in Porous Media **58** (2005), 339–360.
- [32] T. Gaisser, *Cosmic Rays and Particle Physics*. Cambridge University Press. 1990.
- [33] L. Bonechi et al., *Development of the ADAMO detector: test with cosmic rays at different zenith angles*, 29th International Cosmic Ray Conference (2005), 101–104.
- [34] V. Kudryavtsev, *Muon simulation codes MUSIC and MUSUN for underground physics*, Computer Physics Communications **180** (2009), 339–346.
- [35] P. Antonioli et al., *A three-dimensional code for muon propagation through the rock: MUSIC*, Astroparticle Physics **7** (1997), 357–368.
- [36] A. Afghoul et al., *Coiled tubing: the next generation.*, Oilfield Review (2004), 38–57.